UKAEA-CCFE-CP(19)21

N.R.Walkden, B.D.Dudson, C.Ham, F.Militello,
D.Moulton, F.Riva, J.T.Omotani

Particle and heat spreading in the tokamak divertor via turbulent mixing

This document is intended for publication in the open literature. It is made available on the understanding that it may not be further circulated and extracts or references may not be published prior to publication of the original when applicable, or without the consent of the UKAEA Publications Officer, Culham Science Centre, Building K1/0/83, Abingdon, Oxfordshire, OX14 3DB, UK.

Enquiries about copyright and reproduction should in the first instance be addressed to the UKAEA Publications Officer, Culham Science Centre, Building K1/0/83 Abingdon, Oxfordshire, OX14 3DB, UK. The United Kingdom Atomic Energy Authority is the copyright holder.

The contents of this document and all other UKAEA Preprints, Reports and Conference Papers are available to view online free at https://scientific-publications.ukaea.uk/

Particle and heat spreading in the tokamak divertor via turbulent mixing

N.R.Walkden, B.D.Dudson, C.Ham, F.Militello, D.Moulton, F.Riva, J.T.Omotani

This paper has been submitted to
23rd International Conference on Plasma Surface Interactions in Controlled Fusion Devices (PSI), Princeton, NJ, USA, 17-22 June 2018

3D simulations of turbulent mixing in a simplified slab-divertor geometry

N.R.Walkden[a], F.Riva[a], B.D.Dudson[b], C.Ham[a], F.Militello[a], D.Moulton[a], T.Nicholas[a,b] and J.T.Omotani[a]

[a]CCFE-UKAEA, Culham Science Centre, Abingdon, Oxfordshire, OX14 3DB, UK
[b]York Plasma Institute, University of York, Heslington, York, YO10 5DD, UK
Email: Nick.Walkden@ukaea.uk

Abstract

Three-dimensional simulations of plasma turbulence have been run using the STORM module of BOUT++ in a simple slab geometry aimed at representing a single, isolated tokamak divertor leg. Turbulence is driven primarily by the Kelvin-Helmholtz mechanism due to the sheared ExB flow that forms around the separatrix due to strong radial gradients in the sheath potential which arise from strong radial gradients in the electron temperature. The turbulence forms a mixing layer around the separatrix which spreads heat and particles into the private-flux region. The resulting spread of the electron heat flux is within the experimental range measured on MAST. An effective thermal transport coefficient which is approximately 10% of the Bohm value is measured from the simulations. When a transport coefficient of this magnitude is used in a diffusive axisymmetric simulation the time-averaged radial profiles share similar features to the full turbulence simulation.

1. Introduction

The flux of heat and particles to the divertor surface is an important quantity for the operation of tokamak devices. Excessive fluxes may limit machine operation by damaging the surface of the divertor, whilst a precise knowledge of these fluxes allows for better estimation of material erosion rates. Many aspects of tokamak operation are dependent on knowledge profiles at the divertor target, which in turn depend on the competition between perpendicular and parallel transport processes in the scrape-off layer. Whilst parallel transport processes are relatively well captured in two-dimensional axisymmetric fluid transport codes [1], perpendicular transport remains more difficult to account for due to its turbulent nature. In broad terms, the contribution of perpendicular transport to profiles at the divertor surface can be decoupled into processes upstream that populate the SOL with particles and heat, and processes downstream that spread these particles and heat across magnetic fieldlines either further into the SOL or into the private-flux region (PFR). This idea is encapsulated in the Eich function [2]

$$q(s) = \frac{q_0}{2} exp\left(\left(\frac{S}{2\lambda_q}\right)^2 - \frac{x_t}{\lambda_q f_x}\right) erfc\left(\frac{S}{2\lambda_q} - \frac{x_t}{S f_x}\right) + q_{bg} \tag{1}$$

where the upstream and downstream transport processes are captured in the λ_q and S parameters respectively. x_t is the radial coordinate at the target, centred on the separatrix; q_0 and q_{bg} are the peak and background heat fluxes respectively and f_x is the midplane to target poloidal flux expansion factor. The Eich function is routinely used to describe the heat-flux profile at the tokamak divertor in attached conditions, and provides an approximate relationship between the integrated heat flux width, λ_{int}, and the two fitting parameters λ_q and S [3]

$$\lambda_{int} \approx \lambda_q + 1.64S \tag{2}$$

which quantifies the radial extent on the divertor target over which heat is deposited. As λ_q reduces, particularly in high field devices such as ITER [2,4], S may play a greater role in setting the heat-flux profile on the divertor target. It is therefore important to establish the physics underlying S. Upstream transport of particles and heat is mediated, at least in some proportion, by mesoscale turbulent structures termed filaments or blobs [5]. Filament generation and motion is complex, though their relation to profiles in the scrape-off layer can be captured with stochastic models that treat them statistically [6,7,8]. Transport downstream (encapsulated by S in equation (1)) is less well understood. The existence of turbulent fluctuations in the divertor has been demonstrated experimentally with both probe [9,10] and camera based diagnostics [10,11,12], however no first-principles physics based model for this turbulence presently exists. This paper presents simulations designed to investigate the physics underlying these divertor-localised turbulence processes in a simplified simulation geometry.

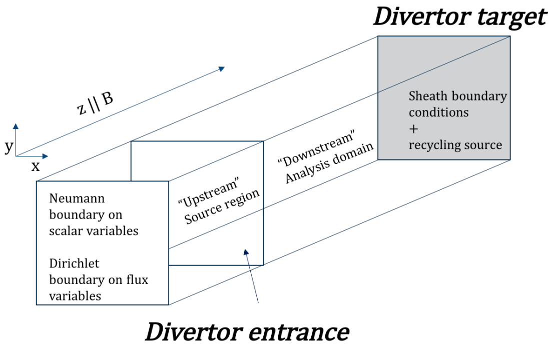
Divertor target
z || B
y
x
Sheath boundary conditions + recycling source
"Downstream" Analysis domain
"Upstream" Source region
Neumann boundary on scalar variables
Dirichlet boundary on flux variables
Divertor entrance

Figure 1: Schematic illustration of the simulation setup used here to simulate a mock-divertor leg. The upstream source region contains density and temperature sources which fall off radially into the SOL, but are zero in the PFR. The downstream region is where analysis is conducted and represents the divertor volume.

2. Simulation setup

The simulation geometry used for this study is a basic field-aligned slab. The x and y dimensions represent the plane perpendicular to the magnetic field and have a well resolved grid resolution with $n_x = n_y = 256$ over a length of $120\rho_s = 43.7cm$. x is the radial coordinate whilst y is a bi-normal coordinate that is perpendicular to both the radial and field-aligned coordinates. The z dimension represents direction parallel to the magnetic field and, due to the field-aligned nature of scrape-off layer turbulence, has a coarse grid with a large grid spacing of $n_z = 20$ over a lengthscale of $1500\rho_s = 5.46m$. A uniform magnetic field strength of 0.25T and a reference temperature of 40eV have been used to represent conditions similar to MAST. The domain is separated into an 'upstream' source region, which fuels the divertor volume and a 'downstream' analysis region. The only difference between the two regions is the presence of axisymmetric density and energy sources in the upstream region. The sources are described by truncated exponential functions such that

$$S_{n,E} = \begin{matrix} S_{n,E}^{bg} + S_{n,E}^{0} \exp\left(-\frac{x}{\lambda_{Sn,E}}\right); & x \geq x_{sep} \\ S_{n,E}^{bg} \qquad\qquad ; & x < x_{sep} \end{matrix} \tag{3}$$

where $S_{n,E}^{bg}$ is a small background source used for numerical stability, $S_{n,E}^{0}$ is the peak in the source at the separatrix and $\lambda_{n,E}$ is the e-folding length, chosen such that the profiles at the divertor target at initialization are experimentally realistic. For the simulations presented here the following values have been used: $S_n^0 = 6.03\times10^{22}m^{-3}s^{-1}$, $S_n^{bg} = 0.05S_n^0$, $\lambda_{Sn} = 24\rho_s = 8.7cm$: $S_E^0 = 5.8MWm^{-3}$, $S_E^{bg} = 0.005S_E^0$, $\lambda_{SE} = 18\rho_s = 6.6\ cm$. This energy influx corresponds to an input power of approximately 1.76MW. At the sheath boundary standard sheath boundary conditions are applied (see [13] for a description). In addition, a recycling source exists in the downstream region which recycles 75% of the ion flux that enters the sheath boundary, Γ_{ion}, back up the same magnetic field line instantaneously over an exponential with an e-folding length of 1m such that

$$S_{rec}(x,z,t) = 0.75\Gamma_{ion}(x,t)\exp(-z). \tag{4}$$

This source attempts to model the recycling of ions from the target heuristically, but does not capture the full interaction between the plasma and a neutral species. Figure 1 shows a schematic illustration of the simulation setup.

The STORM [13,14,15,16] module for BOUT++ [17,18] has been used to conduct these simulations. The module solves a 5-field system of equations for the electron density, n, the electron temperature, T, the electron and ion parallel velocities, V and U respectively, and the vorticity, $\Omega = \nabla_\perp^2\phi$ where ϕ is the electrostatic potential. The potential, ϕ, and conductive parallel heat flux, q_e, are auxiliary variables. The model makes the electrostatic assumption, the cold-ion assumption and the 'Boussinesq' approximation [19]. The full set of equations and their respective boundary conditions at the sheath entrance can be found in [13,16].

To initialize the simulations the code is run in a 2D ‘hydrodynamic’ mode with $V = U$ imposed and perpendicular diffusion coefficients chosen to be physically realistic. In this case, these were set to be 2.5 times their classical values [20]. This provides the initial conditions for the full 3D turbulent simulations. Figure 2 shows examples of the hydrodynamic profiles used here as an initial condition, taken at the sheath entrance.

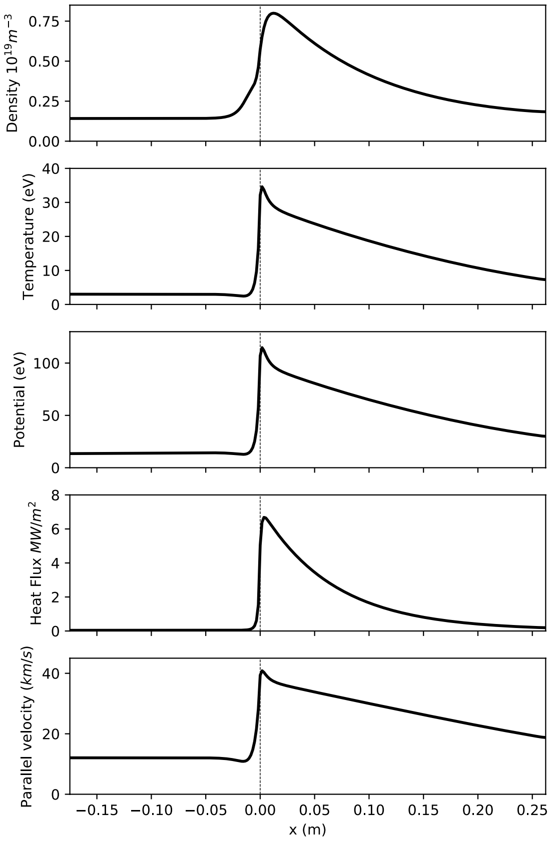

Figure 2: Radial profiles taken from the 2D ‘hydrodynamic’ simulation used as an initial condition for turbulence simulations, plotted here at the sheath boundary.

3. Results

Diagnosing the turbulence

In the initial phases of the simulation, the steep radial profiles that develop from the 2D hydrodynamic initial condition become linearly unstable before developing into fully non-linear turbulence. The linear instability observed to drive the transition into turbulence is the transverse Kelvin-Helmholtz instability [21]. This is confirmed by calculating the growth rate as a function from the full 3D simulation in an early part of the simulation and comparing to a semi-analytic dispersion relation for the Kelvin Helmholtz instability. Isolating only the non-linearity in the vorticity equation (see [13,16]) and linearizing leads to a generalised eigenvalue equation [22],

$$\frac{\omega}{k_\perp} A(\phi) = B(\phi) \tag{5}$$

$$A \equiv \frac{d^2}{dx^2} - k_\perp^2 \tag{6}$$

$$B \equiv v_E A - v_E'' \tag{7}$$

which can be solved for a given $k_\perp$ to obtain the complex mode frequency ω of the Kelvin-Helmholtz instability. The method is semi-analytic because a second-order finite difference scheme has been used to convert the operators A and B into tri-diagonal matrices. The eigenvalues and eigenvectors of the problem are then computed using the *eigvals* solver in the *scipy.linalg* python library. Figure 3 shows the dispersion relation from the simulation compared to the semi-analytic prediction.

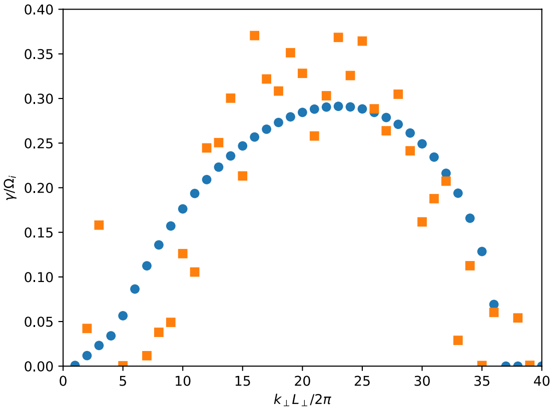

Figure 3: Dispersion relation from the early phase of the full 3D turbulence simulation (orange squares) compared to the semi-analytic calculation using the averaged potential profile at the divertor target (blue circles) from the 3D simulation. Although there is considerable spread in the simulation results, the dispersion relation is highly consistent with a Kelvin-Helmholtz instability.

The comparison between the growthrate calculated in the simulation and semi-analytic case is qualitatively and quantitatively similar, though significant scatter is present in the simulation data. This is likely due to non-linear coupling since, even at early times, many modes are excited by virtue of the broad dispersion relation of the KH instability. It is worth noting that the conditions used for the simulations presented here may be particularly susceptible to the Kelvin-Helmholtz instability. In particular, Myra has shown in a recent study [21] that electromagnetic parallel currents and ion diamagnetic effects, both of which were not implemented in the STORM code at the time of this study, may have a stabilizing effect of the KH instability. The former effect requires high values of the plasma β and low values of resistivity so may be less impactful in the tokamak divertor leg. The latter requires gradients in the ion pressure (leading to shear in the ion diamagnetic velocity) to be comparable to the ExB flow shear. In the divertor leg the initial gradient across the separatrix into the PFR, where the KH mode is driven, is determined primarily by the rate of power loss to the target. Since the electron power loss is more rapid than the ion power loss, the electron temperature gradient will likely be steeper than the ion gradient, leading to a steeper ExB velocity shear than the ion diamagnetic velocity shear. As such, both EM and ion diamagnetic effects may impact the stability observed here, but are unlikely to fully stabilize the system.

Although interesting from the perspective of understanding the physics driving the simulation, the linear phase only provides an initial condition for the true saturated turbulence phase, which is of real importance to this study. It is therefore interesting to investigate the role played by the different terms affecting turbulence during the saturated phase. The turbulence drive in the system can be investigated by artificially eliminating different terms in the vorticity equation. To eliminate the KH mechanism, following Ricci and Rodgers [23], the nonlinear advection term is modified to

$$[\phi, \nabla_\perp^2 \phi] \rightarrow [<\phi>, \nabla_\perp^2 \phi] \qquad (8)$$

where <> represents an average in the y direction. Another drive for turbulence is the interchange mechanism [24], which is thought to play a dominant role in the development of turbulence in the upstream SOL [25]. This can be eliminated from the system by setting the effective gravity to zero. Figure 4 shows cross-sections of the electron pressure and the electrostatic potential at the sheath boundary, compared between three cases: a baseline case (*Full*) where all terms are active, a case where the interchange mechanism is removed (*Intr off*) and a case where the KH mechanism is removed (*KH off*).

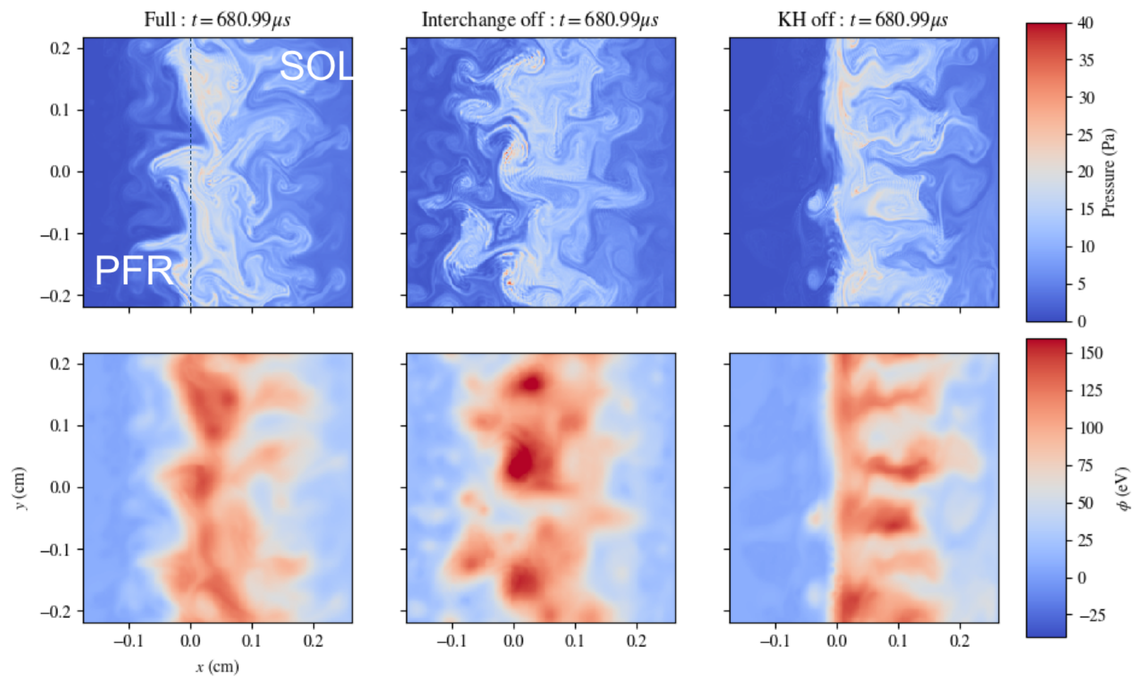

Figure 4: Cross-sections of the electron pressure (upper) and electrostatic potential (lower) during the saturated turbulence phase compared by the three cases with differing turbulence drives. Cross-sections are taken at the sheath boundary. An animated version of this figure is available at [https://drive.google.com/open?id=1F2Cda3LpubXT05gaxovyhozrqd0OA9BS]

Figure 4 shows that the KH mechanism and thus KH turbulence is responsible for the formation of a mixing layer around the separatrix which relaxes gradients into the PFR region. This is intuitive, since in an outer divertor leg the PFR represents a region of ‘good curvature’ where the curvature vector is anti-parallel to the pressure gradient, therefore interchange turbulence is not expected to be present. In the SOL, which represents a ‘bad curvature’ region, some streamer-like structures are present which have a notably longer radial correlation length when the KH mechanism is removed. In a realistic situation turbulence in the outer SOL region is strongly coupled to upstream turbulence [10], and therefore the results obtained here in the outer-SOL region may not be fully relevant to the experimental reality. In the *KH off* off case some residual drift-wave turbulence remains local to the separatrix and the simulation does not fully relax to its 2D initial condition. Nevertheless the narrowing of the mixing layer is dramatic. Figure 5 shows the radial profiles from the turbulent simulations, averaged in time and in the y direction.

Interestingly, although the PFR is an area of ‘good curvature’, the interchange mechanism does play a role as shown in the comparison between the *Full* and *Intr off* case. Particularly the interchange mechanism leads to a partial narrowing of the profiles into the PFR. Since the linear analysis demonstrated the dominance of the KH instability in the *Full* simulation, and since the PFR is a good curvature region where interchange turbulence would not be expected to develop naturally, this indicates that the role played by the interchange mechanism is prevalent only when turbulence has been established via the KH mechanism.

In figure 6 the ExB energy spectrum is compared between the three simulations. Figure 6 indicates that the KH mechanism is responsible for an inverse (enstrophy) cascade [26,27] to larger length scales, limited by transport into the sheath as the turnover time increases in the larger structures. The large-scale structures can then be acted on by the interchange mechanism in a manner similar to filament motion in the upstream SOL [5]. This drives structures that are ejected into the PFR back towards the separatrix leading to the narrowing of the mixing layer. This suggests that the angle of the divertor leg with respect to the curvature vector (which here would be parametrised here in the effective gravity) may have an impact on the width of the mixing layer. A horizontal divertor leg which lies parallel to the curvature vector would be expected to see a reduced impact of the interchange mechanism and thus a widening of the KH mixing layer. This important aspect of these simulations will be followed up in a future report.

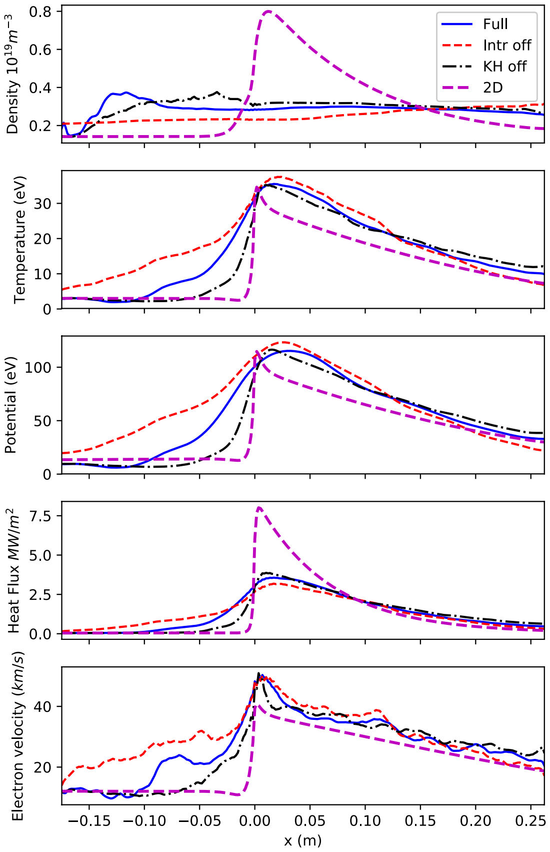

Figure 5: Radial profiles taken from the three comparison turbulence simulations and the 2D hydrodynamic initial conditions.

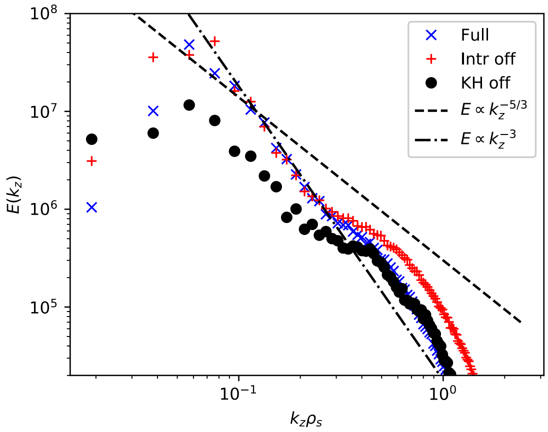

Figure 6: ExB energy spectrum for each of the three comparison cases. The KH mechanism is responsible for an inverse cascade towards larger scales. Structure in the tail of the spectrum is partly the result of numerical artefacts which do not affect the transport properties of the simulation.

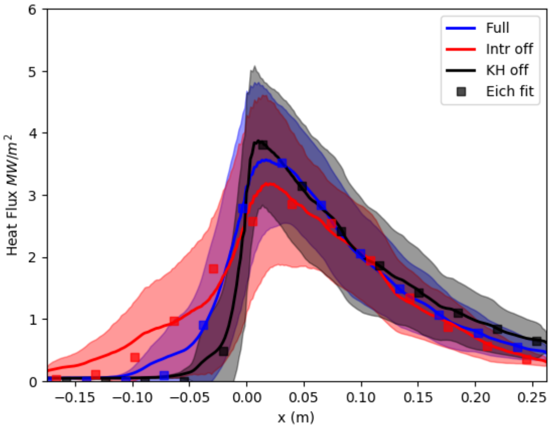

Figure 7: Heat flux profiles at the sheath boundary for each of the three simulations compared here. Square symbols (color coded to their respective profile) show an Eich function fitted to each of the heat flux profiles. The filled areas show one standard deviation either side of the mean profiles due to fluctuations from the turbulence.

Target Heat flux

The width of the mixing layer is echoed in the profile of the electron heat flux (due to the cold ion assumption this is equivalent to the total heat flux in these simulations) at the divertor surface. Figure 7 shows the electron heat flux (including convective and conductive components) for the three simulation. Also shown are the results from fitting the heat flux with an Eich function (equation (1)).

The profile of the heat-flux at the divertor target is well captured by the Eich function. The maximum deviation occurs when the interchange mechanism is removed and the KH turbulence is strongest. The deviation from the Eich fit grows in the far PFR, indicating that turbulent transport provides stronger transport into the far PFR than predicted by the simple diffusion-conduction model of the Eich function. In table 1 the parameters of the Eich fits are given, with a flux expansion factor of $f_x = 10$ which is applicable to the poloidal flux expansion expected from the outboard midplane to the X-point entrance of MAST [28].

Table 1: Parameters obtained from an Eich fit of the target heat flux from each of the three simulations. Typical ranges from MAST L-mode data measured by IR thermography [26]

Case	$\frac{\lambda_q}{f_x}\,(mm)$	$\frac{S}{f_x}\,(mm)$	$q_0(MWm^{-2})$	$q_{bg}(MWm^{-2})$	$x_{sep}(m)$
Full	10.46	4.03	5.72	0.044	-0.011
Intr off	7.60	8.31	7.70	0.143	-0.010
KH off	13.00	1.72	4.72	0.043	-0.005
Typical MAST L-mode ranges	7 - 19	2.1 – 5.8	-	-	-

As expected from the results of the previous section, eliminating the KH turbulence from the system leads to a narrow PFR region and a low value of $\frac{S}{fx}$, whilst eliminating the interchange mechanism leads to a broad PFR and large values of $\frac{S}{fx}$. Although, as already stated, the results in the SOL region may not be directly relatable to experimental conditions it is interesting to note that as the PFR narrows the SOL is broadened due to the increased prevalence of interchange turbulence in the SOL region. The *Full* simulation produces a spreading parameter that is within the range measured on MAST [29, 30]. It is also interesting to note that MAST exhibits a wider heat flux profile on the inner target than on the outer [31] which fits with the predictions made here based on the impact of the interchange mechanism on $\frac{S}{fx}$.

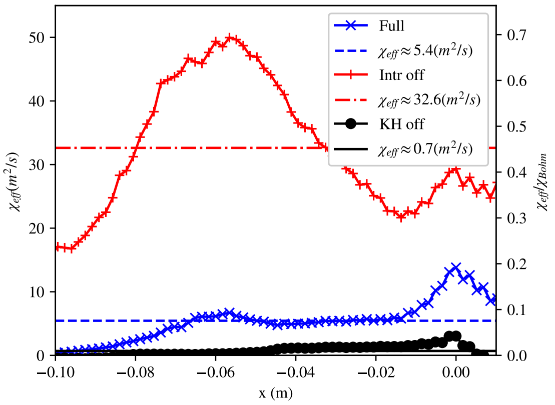

Figure 8: Effective diffusivities from the three comparison simulations in physical dimensions (left axis) and compared to the Bohm diffusivity in the simulations (right axis) in the inner PFR region. Horizontal lines show the average value of the profiles shown for each simulation.

Transport levels

For each simulation, a representative thermal diffusion coefficient can be obtained by calculating

$$\chi_{eff} \approx \frac{\Gamma_p}{p'} \tag{9}$$

where

$$\Gamma_p = v_{x,ExB}\, p \tag{10}$$

is the thermal ExB flux which is averaged in the y and in time. Figure 8 shows the measured χ_{eff} in the inner PFR region in both dimensional units and normalised to the Bohm diffusivity, alongside its average in the radial span shown.

The effective thermal diffusivity measured in the *Full* simulation is approximately 10% of the Bohm diffusivity and has a value within the range of diffusivities estimated with target ion saturation current data on MAST [32]. As expected, the *Intr off* simulation shows a much higher effective diffusivity without the interchange mechanism counterbalancing the KH turbulence. The increase in χ_{eff} is around a factor of 6, whilst the increase in S/f_x is much more modest at a factor of 1.9. As the temperature and density in the PFR rise due to the turbulent transport, the heat loss through the sheath also rises because of its dependence on n and T, so the impact on the spreading factor, S/f_x, is reduced.

The effective diffusivity measured in the simulation is certainly not constant radially. A constant diffusion coefficient is a common assumption in axi-symmetric transport modelling of the SOL and it is therefore useful to assess how well such an assumption can capture features of the fully turbulent simulation. To perform this comparison, the code was re-run in hydrodynamic mode (as described in section 2) using a diffusive transport coefficient of 0.1 χ_{Bohm} for both the particle and thermal diffusivities. Figure 9 compares the time and y-averaged profiles of the density, temperature and parallel heat flux between the *Full* turbulent simulation and the hydrodynamic simulation. The profiles are color-coded to their position along the magnetic field line.

Whilst not being able to capture some finer detail of the profile structures, the diffusive approximation does an adequate job of capturing the broadening of the heat flux into the PFR. This suggests that, if diffusion coefficients can be appropriately chosen, then the diffusive transport approximation may be justified in modelling the heat spreading in the divertor leg. It is worth noting that this is in stark contrast to the case of the upstream SOL, where cross-field transport is robustly non-diffusive [33, 34].

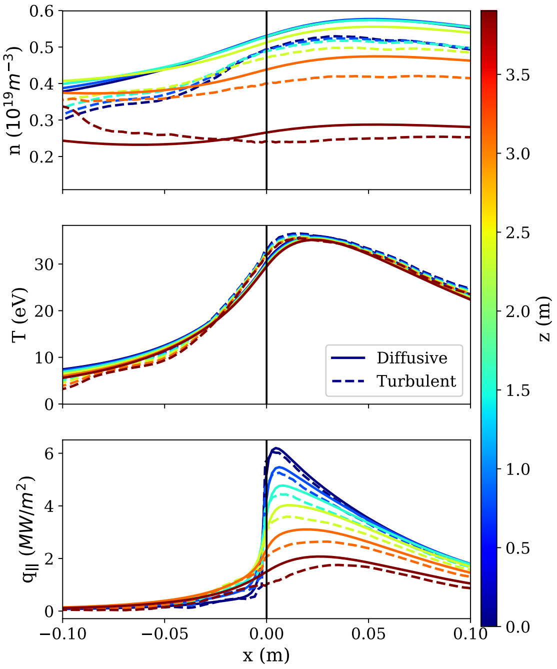

Figure 9: Comparison of the density, temperature and conductive heat flux steady state profiles between the *Full* turbulent simulation and a diffusive simulation with a $\chi = 0.1\chi_{Bohm}$. The color coding represents different positions along the magnetic field line from the X-point entrance (Z = 0) to the sheath boundary.

4. Summary

This paper has presented simulations of turbulence in a simplified geometry aimed at representing a single isolated tokamak divertor leg using the STORM module of BOUT++. The simulations are initialised with conditions that satisfy a hydrodynamic steady state with transport coefficients that are near the classical values. These conditions are unstable to a linear Kelvin-Helmholtz instability, though the broad dispersion relation leads to mode coupling even in the early stages of the simulation. In the saturated turbulence phase the turbulence is sustained by the Kelvin-Helmholtz mechanism. This is demonstrated by comparing simulations with both the Kelvin-Helmholtz and interchange mechanism artificially removed in turn. The interchange mechanism has a regulatory effect on the turbulence by acting on large scale structures that appear in the PFR due to the turbulence and driving them back towards the SOL. The heat flux profiles at the divertor target produced from the full simulation show spreading into the private-flux region that is comparable to experimental ranges measured on MAST. Effective transport coefficients are estimated from the simulation in the inner PFR region and are approximately $\chi \approx 0.1\chi_{Bohm}$, again within the range of experimental estimates for MAST. Finally a diffusive, axisymmetric simulation is run with these transport coefficients used and the resulting profiles are similar to the time and poloidally averaged profiles from the turbulent simulation, though some finer details in the profiles are not recovered. This suggests that in the divertor volum, the diffusive approximation may be adequate for capturing the important aspects of radial transport due to turbulence, in contrast to upstream SOL turbulence which is robustly non-diffusive. A fuller description of this study will be released in a future report.

Acknowledgements

This work has been carried out within the framework of the EUROfusion Consortium and has received funding from the Euratom research and training programme 2014-2018 under grant agreement No 633053 and from the RCUK Energy Programme [grant number EP/P012450/1]. NRW gratefully acknowledges funding and support through EUROfusion researcher grant AWP16-ERG-CCFE/Walkden. The simulations presented here were carried out on the CINECA Marconi supercomputer under the SOL_BOUT project. To obtain further information on the data and models underlying this paper please contact PublicationsManager@ccfe.ac.uk. The views and opinions expressed herein do not necessarily reflect those of the European Commission.

References

[1] E.Havlickova, W.Fundamenski, F.Subba, D.Coster, M.Wischmeir and G.Fishpool, *Plasma Phys. Control. Fusion*, **55** (2013) 065004

[2] T.Eich, A.W.Leonard, R.A.Pitts *et. al., Nuclear Fusion*, **53** (2013) 093031

[3] M.A.Makowski, D.Elder, T.K.Gray *et. al., Phy. Plasmas,* **19** (2012) 056122

[4] T.Eich, B.Sieglin, A.Scarabosio *et. al., Phys. Rev. Lett.*, **107** (2011) 215001

[5] D.A.D'Ippolito, J.R.Myra and S.J.Zweben, *Phys. Plasmas*, **18** (2011) 060501

[6] F.Militello and J.T.Omotani, *Nuclear Fusion,* **56** (2016) 104004

[7] F.Militello and J.T.Omotani, *Plasma Phys. Control. Fusion,* **58** (2016) 125004

[8] F.Militello, T.Farley, K.Mukhi, N.R.Walkden and J.T.Omotani, *Phys. Plasmas*, **25** (2018) 056112

[9] I.Garcia-Cortes *et. al.*, *Plasma Phys. Control. Fusion*, **38** (1996) 2051

[10] N.R.Walkden, J.Harrison, S.A.Silburn *et. al., Nuclear Fusion* **57** (2017) 126028

[11] J.R.Harrison, G.M.Fishpool, A.J.Thornton and N.R.Walkden, *Phys. Plasma* **22** (2015) 092508

[12] R.J.Maqueda and D.P.Stotler, *Nuclear Fusion*, **50** (2010) 075002

[13] N.R.Walkden, L.Easy, F.Militello and J.T.Omotani, *Plasma Phys. Control. Fusion*, **58** (2016) 115010

[14] L.Easy, F.Militello, J.T.Omotani *et. al., Phys. Plasmas*, **21** (2014) 122515

[15] J.T.Omotani, F.Militello, L.Easy and N.R.Walkden, *Plasma Phys. Control. Fusion*, **58** (2016) 014030

[16] F.Militello, N.R.Walkden, T.Farley *et. al., Plasma Phys. Control. Fusion*, **58** (2016) 105002

[17]B.D.Dudson *et. al.*, *Comp. Phys. Comm.,* **180** (2009) 1467

[18]B.D.Dudson *et. al., Journ. Plasma Phys.,* **81 (**2015) 1

[19] J.R.Angus and M.V.Umansky, *Phys. Plasma.,* **21** (2014) 012514

[20] S.I.Braginskii, *Rev. Modern Phys. Vol 1*, 1965 (New York: Consultants Bureau) p. 205

[21] J.R.Myra, D.A.D'Ippolito, D.A.Russell, M.V.Umansky and D.A.Baver, *J. Plasma Phys,* **82** (2016) 905820210

[22] K.Lotov, D.Ryutov and J.Weiland, *Physica Scripta*, **50** (1994) 153 – 160

[23] B.N.Rogers and P.Ricci, *Phys. Rev. Lett.,* **104** (2010) 225002

[24] O.E.Garcia, N.H.Bian and W.Fundamenski, *Phys. Plasmas*, **13** (2006) 082309

[25] O.E.Garcia, V.Naulin, A.H.Nielsen and J.Juul.Rasmussen, *Phys. Rev. Lett.*, **92** (2004) 165003

[26] R.H.Kraichnan, *Phys. Fluids*, **10** (1967) 1417

[27] R.H.Kraichnan and D.Montgomery, *Rep. Prog. Phys,* **43** (1980) 548

[28] D.Moulton, J.Harrison, B.Lipschultz and D.Coster, *Plasma Phys. Control. Fusion,* **59** (2017) 065011

[29] S.Elmore *et. al,* "Scaling of the scrape-off layer width in MAST L-mode plasmas as measured by infrared thermography", 45th EPS conference on Plasma Physics, Prague (2018)

[30] A.J.Thornton and A.Kirk, *Plasma Phys. Control. Fusion*, **56** (2014) 055008

[31] F.Militello *et. al., Nuclear Fusion,* **56** (2015) 016006

[32] J.Harrison, G.M.Fishpool and A.Kirk, *Journ. Nucl. Mater.,* **438** (2013) S375

[33] O.E.Garcia *et. al., Journ. Nucl. Mater.*, **363 - 365** (2007) 575

[34] V.Naulin *et. al., Journ. Nucl. Mater.,* **363 – 365** (2007) 24